Supplementary Information (SI) for Nanoscale.

Supplementary Information

Direct thermal atomic layer deposition of high-*κ* dielectrics on monolayer MoS_2: nucleation and growth

Brendan F. M. Healy, Sophie L. Pain, Nicholas E. Grant, and John D. Murphy**

School of Engineering, University of Warwick, Coventry, CV4 7AL, United Kingdom

*** Corresponding Authors**

Brendan F. M. Healy - Email: brendan.f.m.healy@warwick.ac.uk

John D. Murphy - Email: john.d.murphy@warwick.ac.uk

Contents

S1. Characterisation of untreated 1L MoS_2

We verify the single-layer nature of the as-received chemical vapour deposited (CVD)-monolayer molybdenum disulfide (1L MoS_2) films *via* atomic force microscopy (AFM) and Raman spectroscopy.

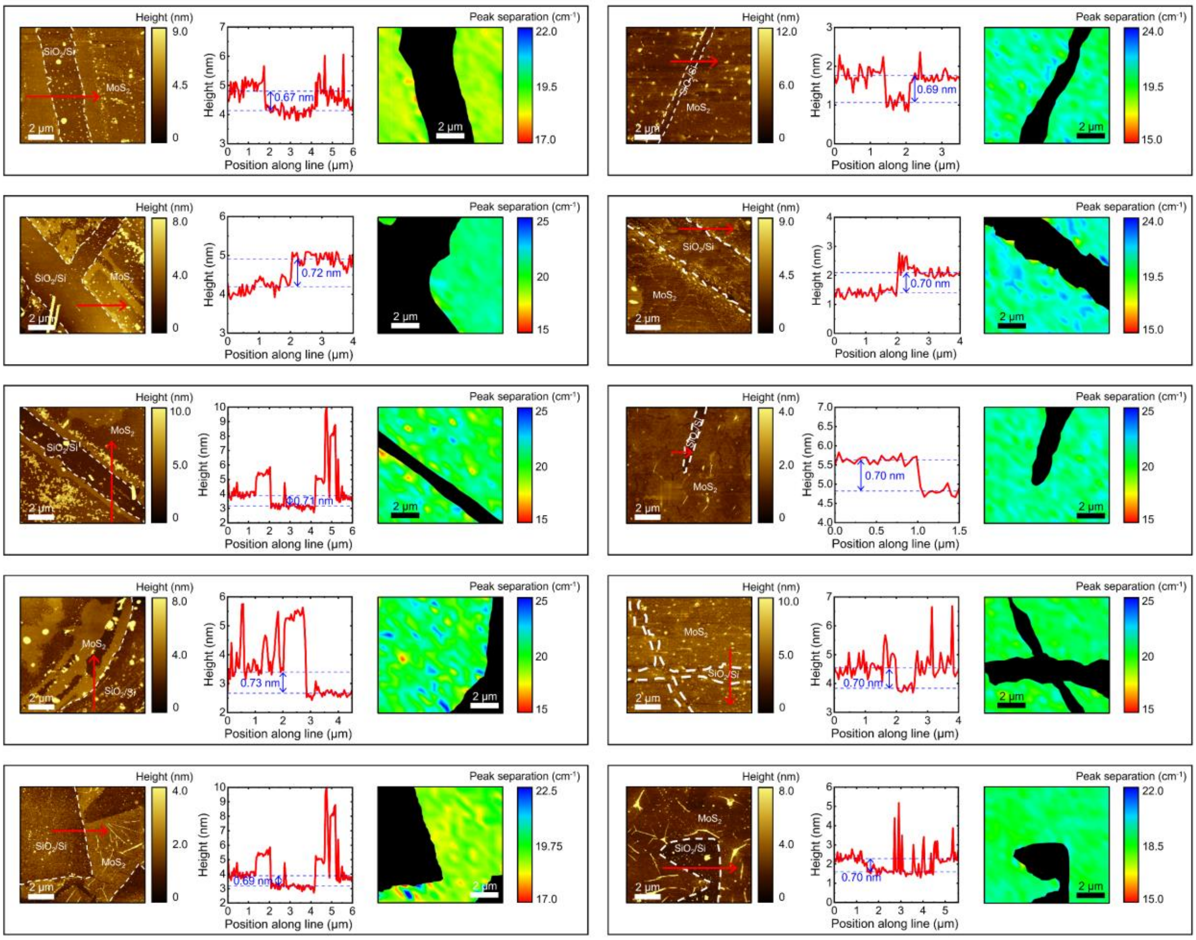

Figure S1: AFM images, line profiles, and maps of the Raman peak separation measured from each untreated 1L MoS_2 film used in this study. In each AFM image, the red arrow indicates the line from which the profile was extracted.

Figure S1 presents low-magnification topographic AFM images and maps of the Raman peak separation measured from each CVD-1L MoS_2 film used in this study prior to any dielectric growth. We trace height profiles across the MoS_2 films and their boundaries with the silicon dioxide/silicon (SiO_2/Si) substrate. Any surface contaminant features of significant height are excluded from the step height estimation, and we obtain step heights of ~0.7 nm in each case, in excellent agreement with the expected thickness of CVD-1L MoS_2.[1-3] The spatially-resolved Raman mapping data further to confirm the single-layer nature of the MoS_2 films. 1L MoS_2 exhibits a distinct Raman signature comprising two characteristic modes: an in-plane E^1_{2g}

vibration at ~384 cm^{-1} and an out-of-plane A_{1g} feature at ~403 cm^{-1}.[4] The separation between these two peaks serves as a robust indicator of monolayer thickness, typically ~18-22 cm^{-1}.[5, 6]

S2. Further AFM images of ALD-Al_2O_3 and -HfO_2 films

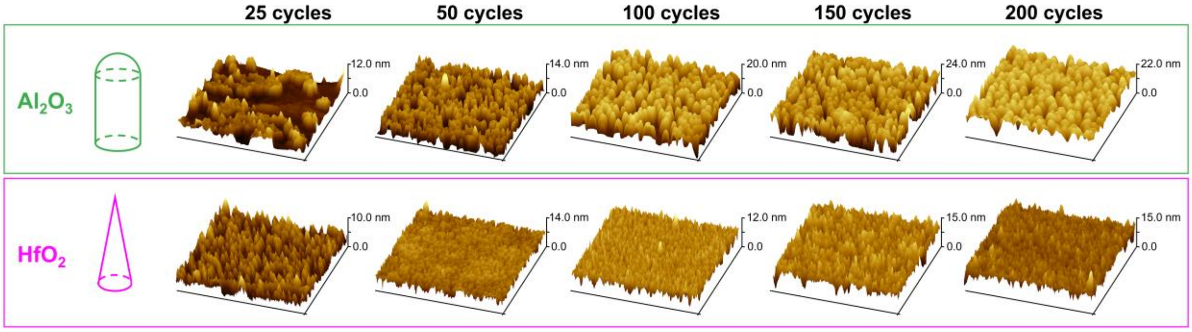

Figure S2: Three-dimensional (3D) atomic force microscopy (AFM) images of the atomic layer deposited (ALD)-aluminium oxide (Al_2O_3) and -hafnium dioxide (HfO_2) films deposited on monolayer molybdenum disulfide (1L MoS_2) at different numbers of ALD cycles as shown in Figures 1 and 2 in the main text. The general shapes of the islands in each dielectric film are also indicated: cylindrical with a hemisphere on top for Al_2O_3 and conical for HfO_2.

S3. Evaluation of island height in ALD-Al_2O_3 film grown after 200 cycles

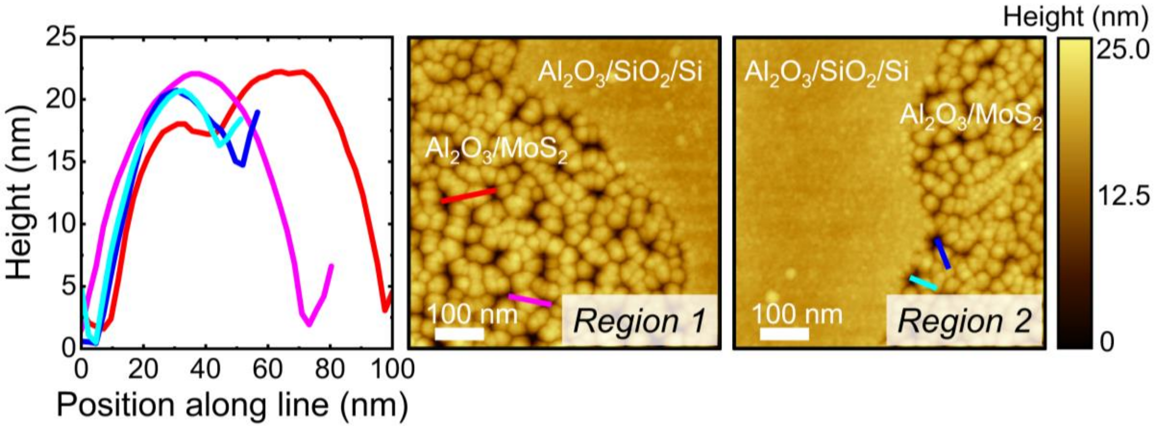

Figure S3: Line profiles from AFM traced across isolated Al_2O_3 islands from two regions of the 1L MoS_2 sample subjected to 200 cycles of ALD-Al_2O_3. These areas are close to edges of the MoS_2 film, where adjacent regions of the underlying silicon dioxide/silicon (SiO_2/Si) substrate experience uniform growth of Al_2O_3. The average height of the Al_2O_3 islands on MoS_2 is determined to be ~20.3 ± 0.2 nm.

S4. Estimation of ALD-HfO_2 thickness on 1L MoS_2

To estimate the thickness of significantly coalesced ALD-HfO_2 films on 1L MoS_2, we utilise companion MoS_2-free SiO_2/Si samples. At each number of ALD cycles of HfO_2, a companion SiO_2/Si wafer was placed in the ALD chamber alongside the 1L MoS_2 sample, and both were simultaneously subjected to the identical growth recipe. The initial thickness of SiO_2 on the companion SiO_2/Si wafers was ~300 nm. Immediately before undergoing ALD, each companion SiO_2/Si wafer was briefly immersed in ~2-3% hydrofluoric acid (HF) for ~1 min, removing the top few nm of thermal oxide and reducing the SiO_2 thickness to be comparable to the ~285 nm-thick SiO_2 that supports the CVD-1L MoS_2 films. Following ALD, spectral reflectivity was used to evaluate the thickness of ALD-HfO_2 on each companion SiO_2/Si wafer, as detailed in the Experimental section in the main text. The thickness of HfO_2 deposited on the uncovered regions of the SiO_2/Si substrate on each 1L MoS_2 sample, d_{sub}, was then assumed to be equal to the thickness measured on the corresponding companion wafer. Following low-magnification AFM imaging of each 1L MoS_2 sample after ALD of HfO_2, we traced line profiles across the boundary between HfO_2/MoS_2 and HfO_2/SiO_2/Si regions to obtain a step height, *H*. At 50 and 100 ALD cycles, the HfO_2 on 1L MoS_2 was found to be thicker than on the surrounding SiO_2/Si regions, while at 150 and 200 ALD cycles, the thickness of HfO_2 was greater on SiO_2/Si. The expected thickness of such CVD-grown 1L MoS_2, *D*, is ~0.7 nm,[7, 8] and we confirm this is true of our untreated 1L MoS_2 samples by extracting line profile information from the AFM. We then infer the thickness in nm of HfO_2 on 1L MoS_2, d_{1L}, *via*:

$$d_{1\mathrm{L}} = d_{\mathrm{sub}} - D - H \qquad \text{(S1)}$$

The parameters in Equation S1 are defined schematically in Figure S4a, and the values obtained at each number of ALD cycles studied here are given in Table S1. To obtain *H*, the relative height of HfO_2 on 1L MoS_2 extracted from the line profile was averaged across the varying islands. Figure S4b presents the thickness of HfO_2 measured on the companion SiO_2/Si wafers at each ALD cycle number. Low-magnification AFM images before and after ALD of HfO_2 at 50 to 200 cycles are displayed in Figure S5, with representative line profiles indicated. For each number of ALD cycles, at least three different line profiles were traced across the 1L MoS_2 sample, with an average of the corresponding step heights calculated.

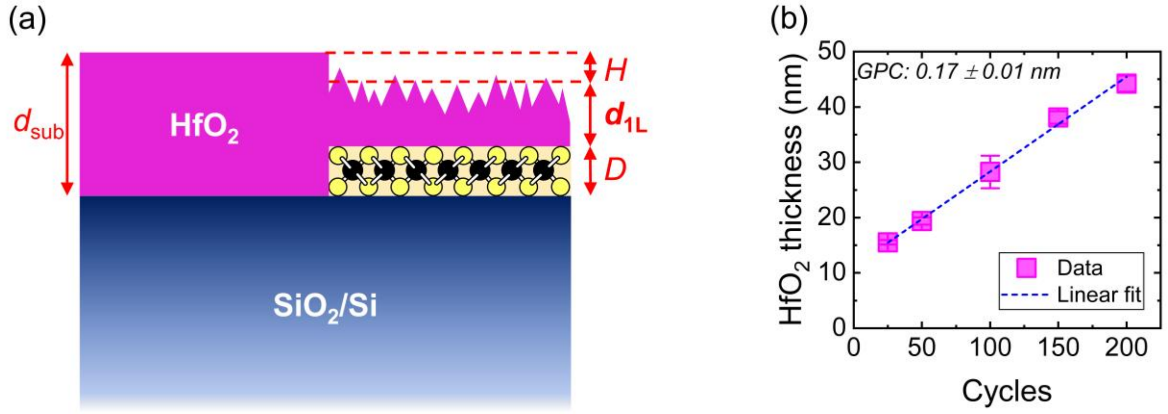

Figure S4: (a) Schematic representation of the thicknesses used to infer the thickness of HfO_2 on 1L MoS_2. This image is not drawn to scale. Note that the step height, H, depicted here is positive but at 50 cycles and 100 cycles, the ALD-HfO_2 on 1L MoS_2 was thicker than on SiO_2/Si, giving negative values of H. (b) HfO_2 film thickness determined via spectral reflectivity as a function of the number of ALD cycles. The gradient of a linear line of best fit is taken to be the growth per cycle (GPC).

Table S1: Summary of the parameters used to infer the thickness of ALD-HfO_2 grown on 1L MoS_2 at each number of ALD cycles.

Number of ALD cycles	d_{sub} (nm)	D (nm)	H (nm)	$d_{1\mathrm{L}}$ (nm)
50	19.4 ± 0.7	0.70 ± 0.05	-3.51 ± 0.28	22.19 ± 0.72
100	28.3 ± 2.9	0.70 ± 0.08	-3.10 ± 0.21	30.65 ± 2.95
150	38.1 ± 1.1	0.70 ± 0.07	0.94 ± 0.67	36.47 ± 1.30
200	44.2 ± 1.5	0.70 ± 0.07	0.82 ± 0.32	42.70 ± 1.50

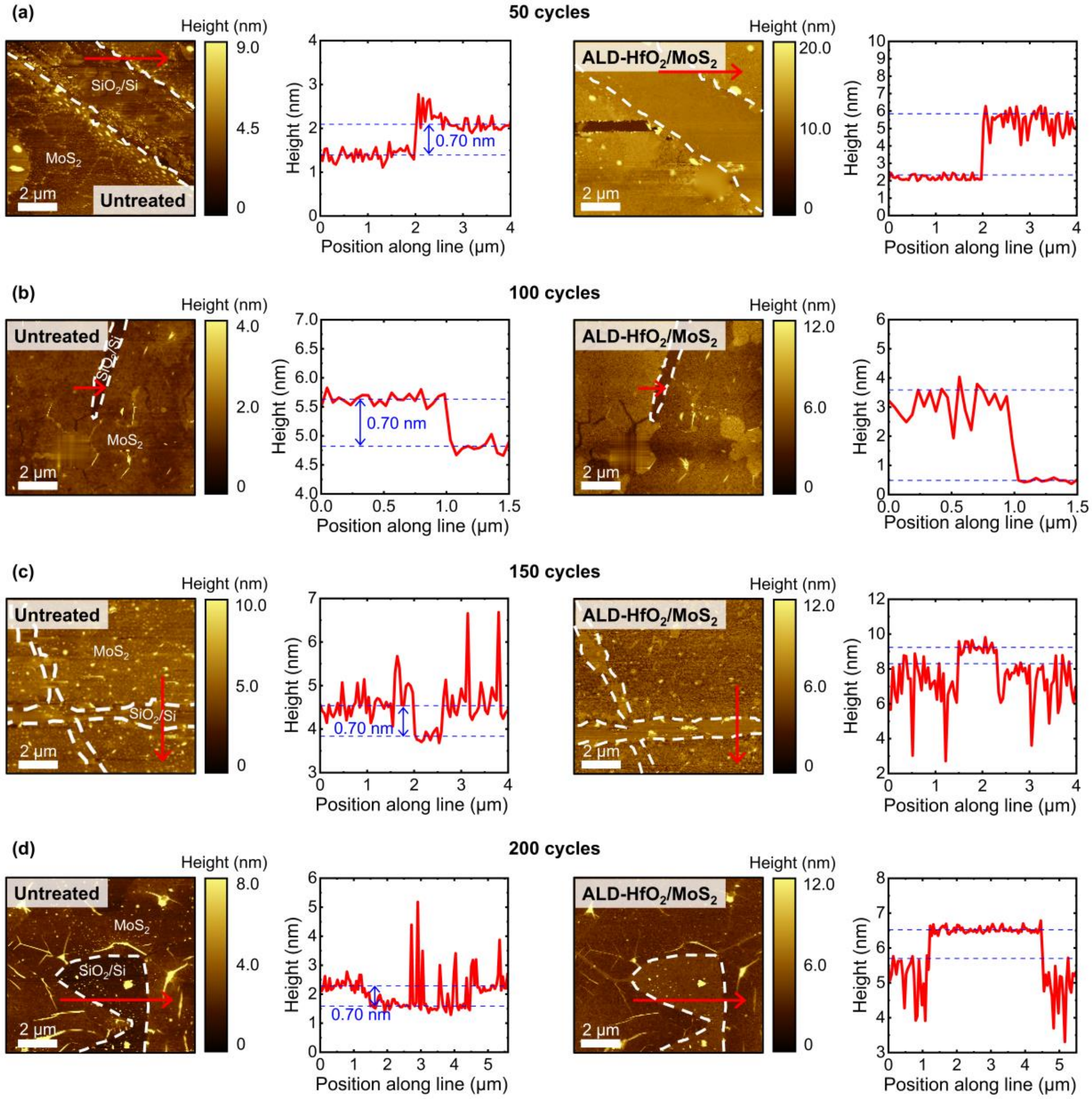

Figure S5: Low magnification AFM images of the surface of each 1L MoS_2 sample before (first column) and after (third column) ALD of HfO_2 at (a) 50 cycles, (b) 100 cycles, (c) 150 cycles, and (d) 200 cycles. For each AFM image, a representative line profile is shown and is plotted to the right of the image. For verification of the CVD-1L MoS_2 thickness, any surface contaminant features of significant height were excluded from the estimation.

S5. PL mapping data

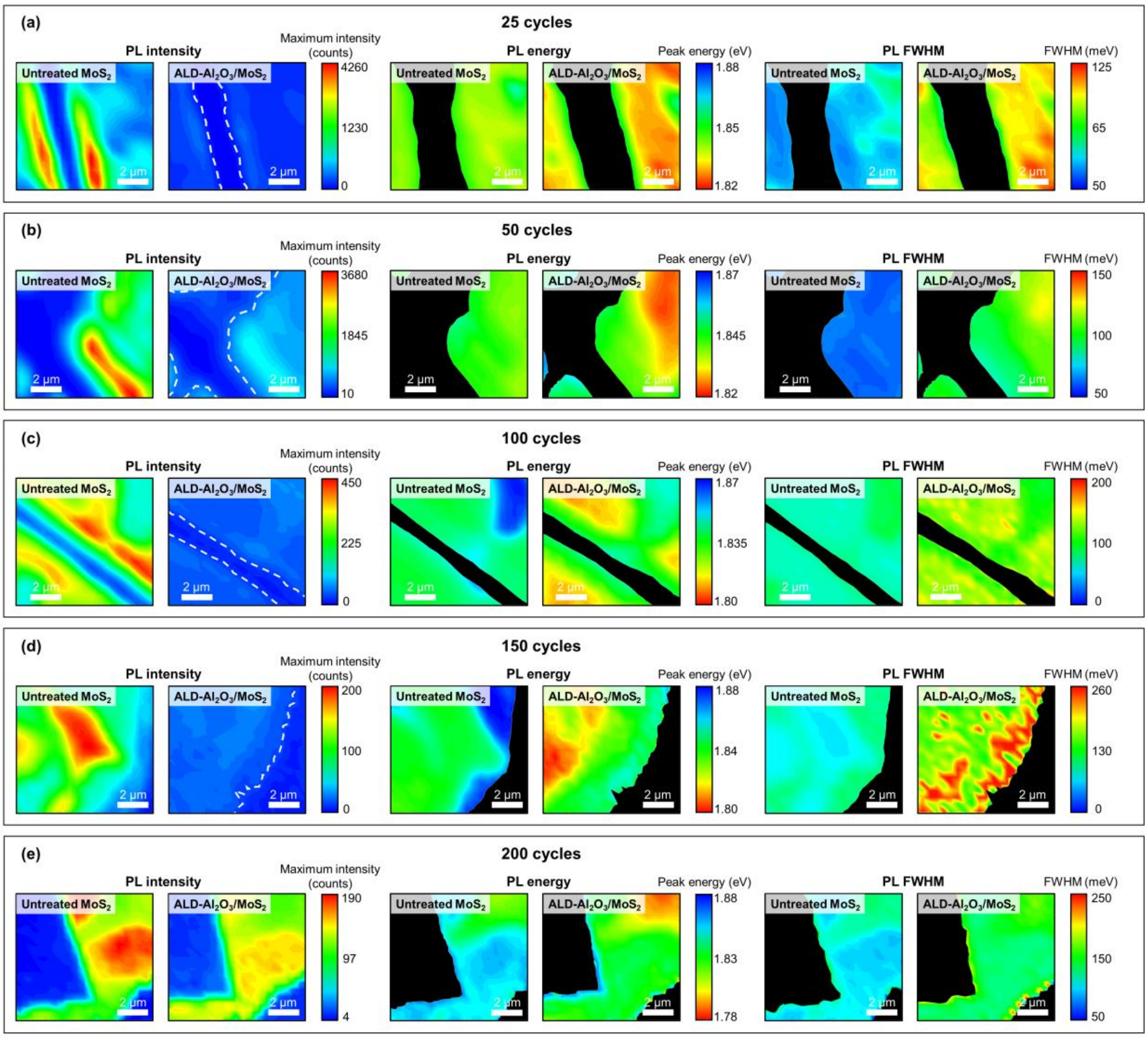

Figure S6: Maps of maximum absolute PL intensity, peak PL energy and FWHM of the PL signal emitted from 1L MoS$_2$ before and after ALD of Al$_2$O$_3$ at cycle numbers (a) 25, (b) 50, (c) 100, (d) 150, and (e) 200. The black areas represent the silicon dioxide/silicon (SiO$_2$/S$_i$) substrate where no MoS$_2$ PL signal is detected.

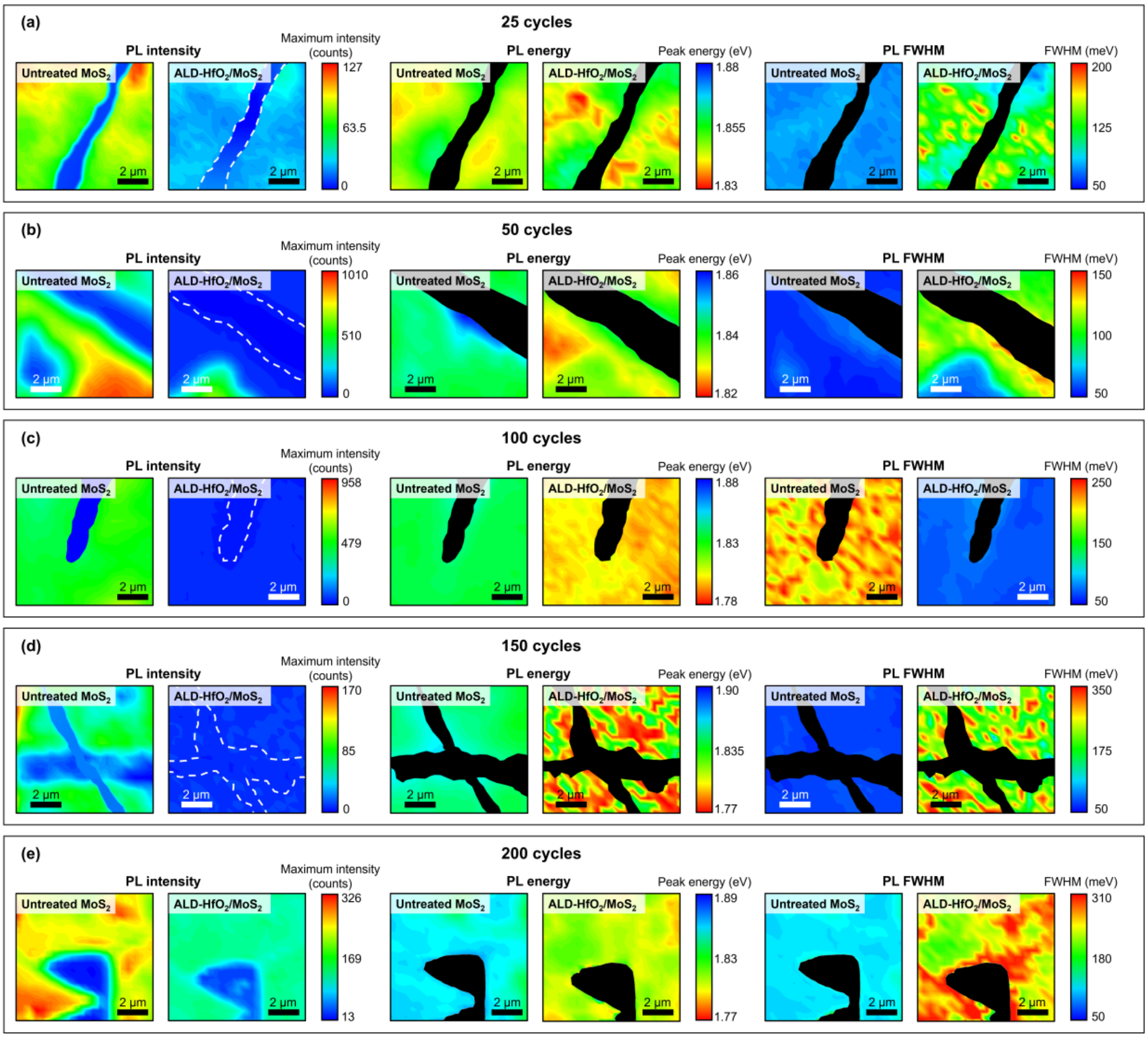

Figure S7: Maps of maximum absolute PL intensity, peak PL energy and FWHM of the PL signal emitted from 1L MoS_2 before and after ALD of HfO_2 at cycle numbers (a) 25, (b) 50, (c) 100, (d) 150, and (e) 200. The black areas represent the SiO_2/S_i substrate where no MoS_2 PL signal is detected.

S6. Deconvolution of single-spot PL spectra

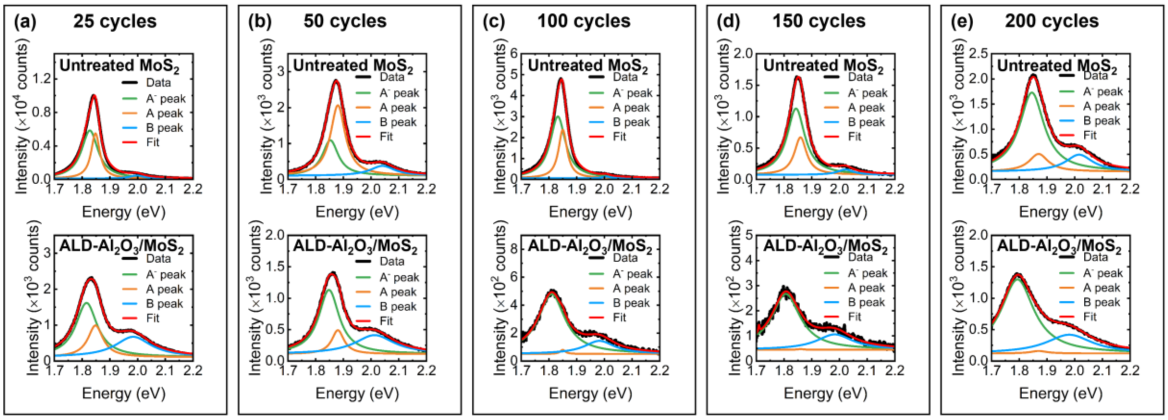

Figure S8: Multipeak deconvolution of the PL spectrum obtained from 1L MoS$_2$ before (top) and after (bottom) ALD of Al$_2$O$_3$ at different cycle numbers. The cumulative fit, and contributions of the A$^-$, A, and B peaks are given in red, green, orange, and blue, respectively.

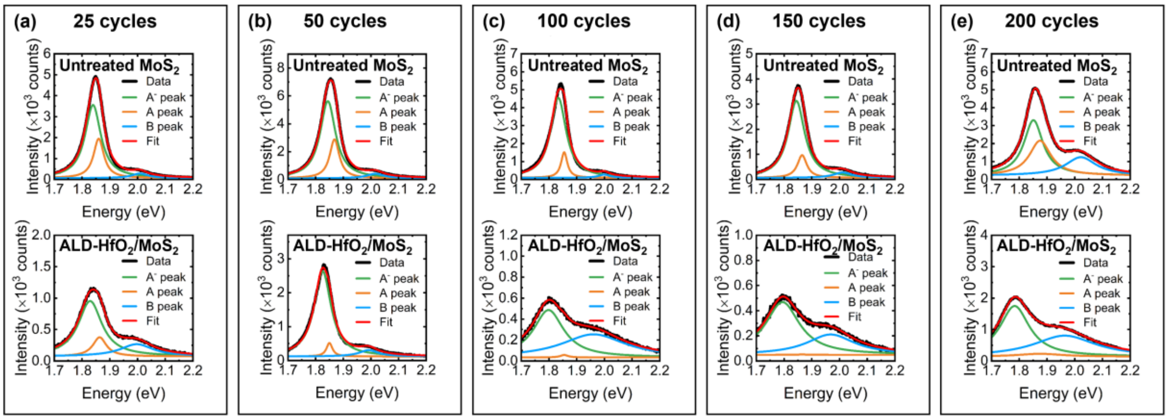

Figure S9: Multipeak deconvolution of the PL spectrum obtained from 1L MoS$_2$ before (top) and after (bottom) ALD of HfO$_2$ at different cycle numbers. The cumulative fit, and contributions of the A$^-$, A, and B peaks are given in red, green, orange, and blue, respectively.

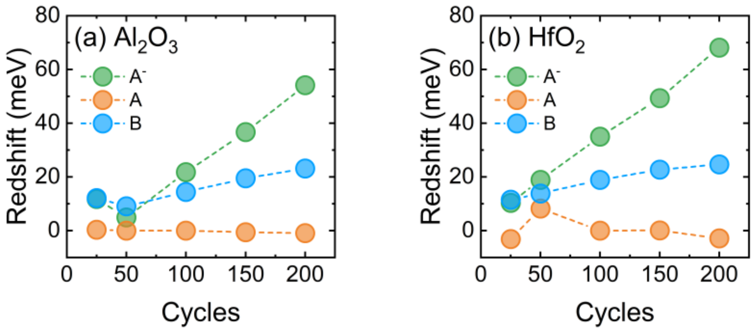

Figure S10: Redshifts of the energy positions of the deconvoluted A$^-$, A, and B PL peaks as a function of ALD cycles for ALD of (a) Al$_2$O$_3$ and (b) HfO$_2$.

S7. Single-spot Raman spectra and Raman mapping data

(a) ALD of Al_2O_3

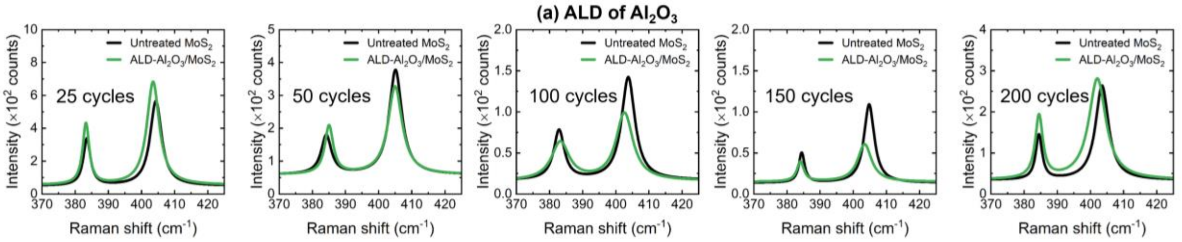

(b) ALD of HfO_2

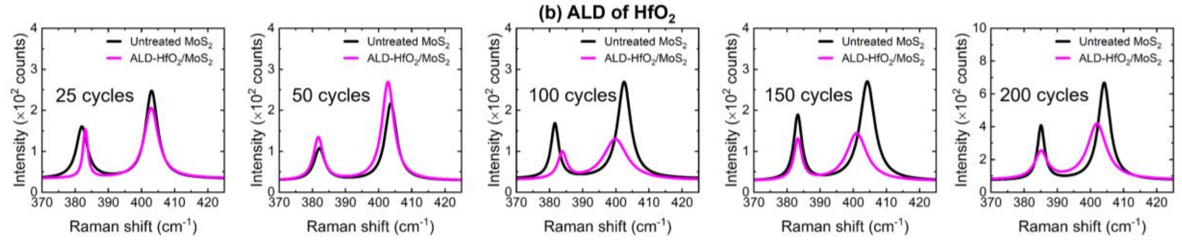

Figure S11: Lorentzian fitting of single-spot Raman spectra measured from each 1L MoS_2 *sample before (black) and after ALD of (a)* Al_2O_3 *(green) and (b)* HfO_2 *(magenta) at each number of ALD cycles.*

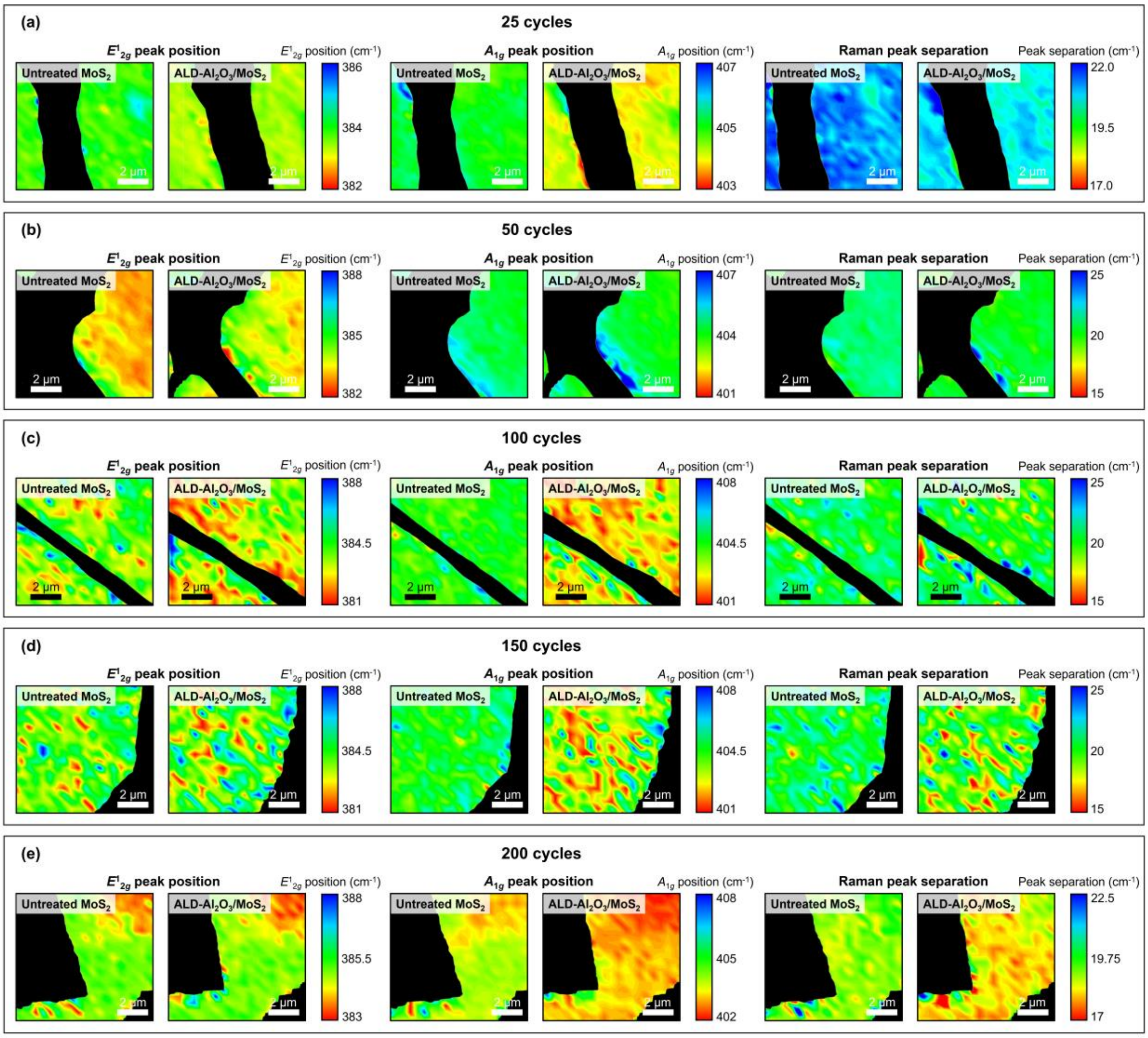

Figure S12: Maps of the E^1_{2g} peak position, A_{1g} Raman peak position, and the Raman peak separation measured from 1L MoS_2 before and after ALD of Al_2O_3 at cycle numbers (a) 25, (b) 50, (c) 100, (d) 150, and (e) 200. The black areas represent the SiO_2/Si substrate where no MoS_2 Raman peaks are detected.

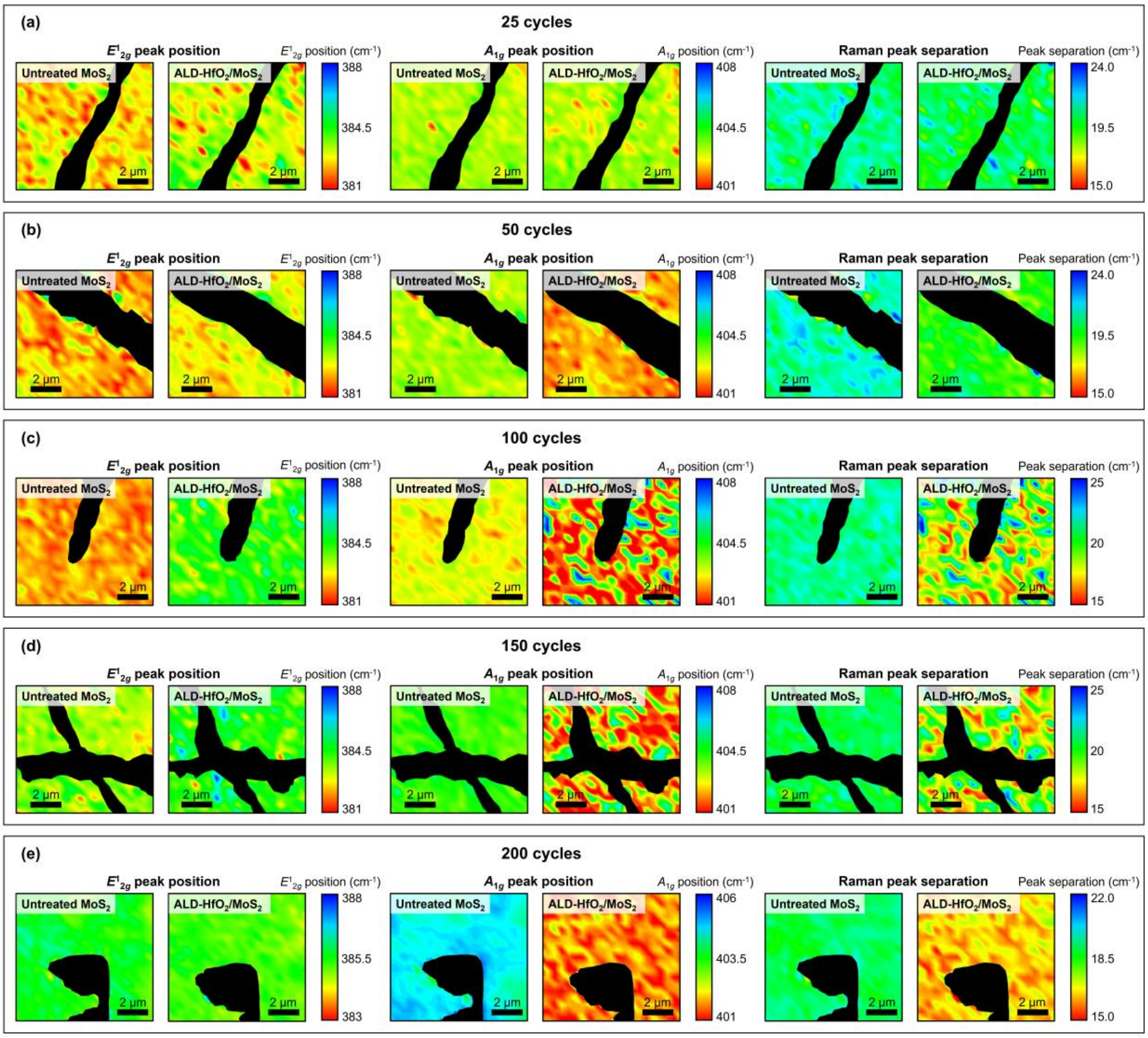

Figure S13: Maps of the E^1_{2g} peak position, A_{1g} Raman peak position, and the Raman peak separation measured from 1L MoS_2 before and after ALD of HfO_2 at cycle numbers (a) 25, (b) 50, (c) 100, (d) 150, and (e) 200. The black areas represent the SiO_2/Si substrate where no MoS_2 Raman peaks are detected.

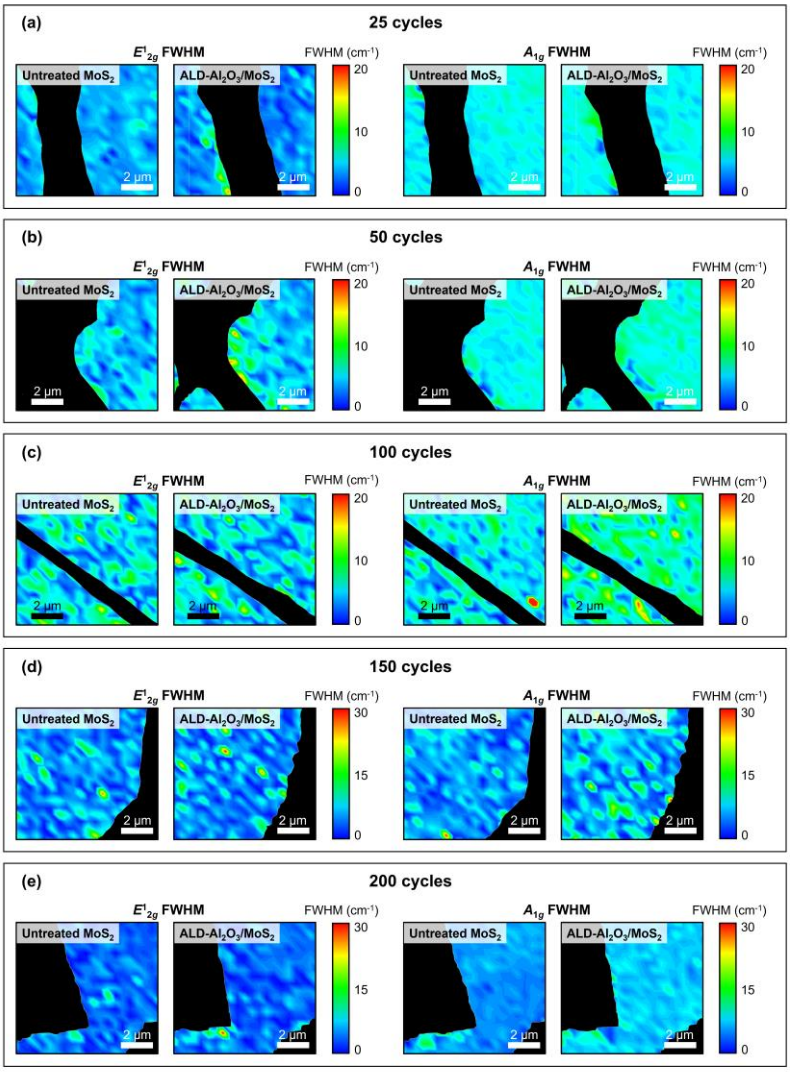

Figure S14: Maps of the FWHM of the E^1_{2g} and A_{1g} Raman peak positions measured from 1L MoS_2 before and after ALD of Al_2O_3 at cycle numbers (a) 25, (b) 50, (c) 100, (d) 150, and (e) 200. The black areas represent the SiO_2/Si substrate where no MoS_2 Raman peaks are detected.

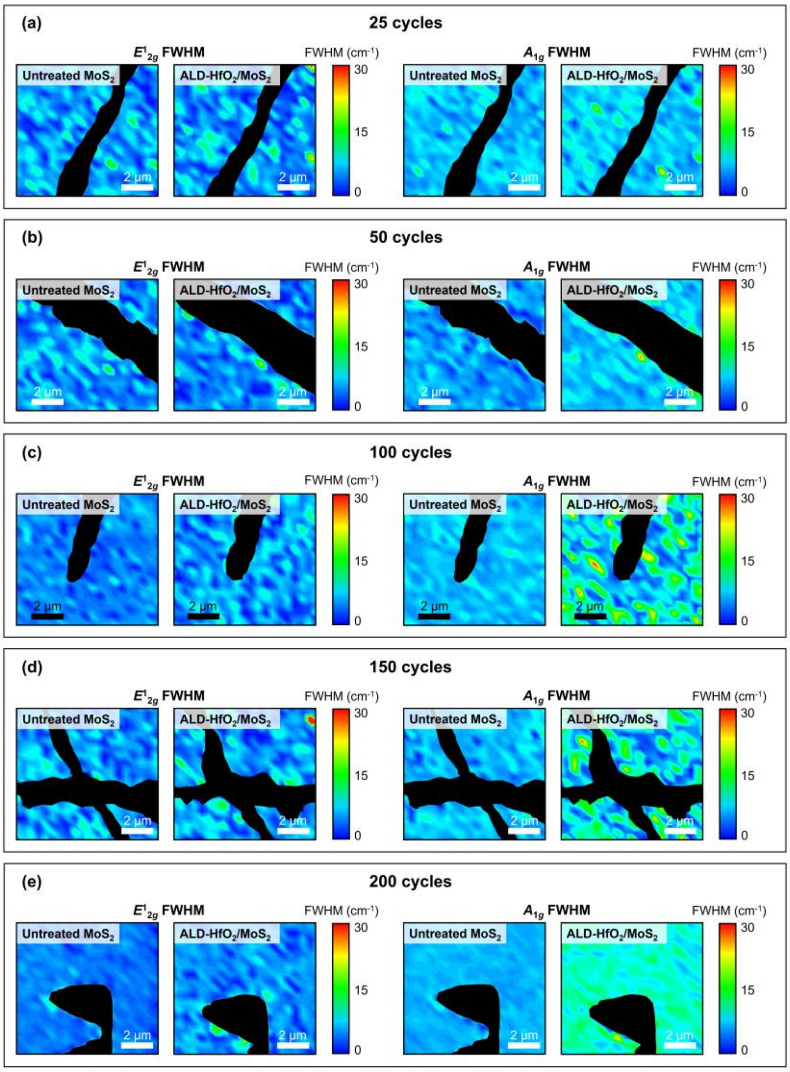

Figure S15: Maps of the FWHM of the E^1_{2g} and A_{1g} Raman peak positions measured from 1L MoS_2 before and after ALD of HfO_2 at cycle numbers (a) 25, (b) 50, (c) 100, (d) 150, and (e) 200. The black areas represent the SiO_2/Si substrate where no MoS_2 Raman peaks are detected.

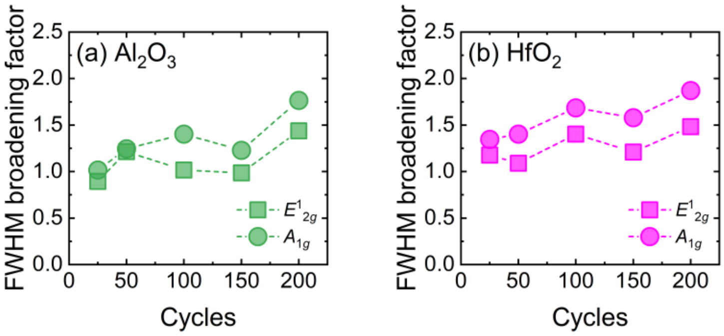

Figure S16: FWHM broadening factors of the E^1_{2g} and A_{1g} Raman peaks extracted from the mapping data as a function of ALD cycles for ALD of (a) Al_2O_3 and (b) HfO_2. The FWHM broadening factor is defined as the ratio of the FWHM of each Raman peak after ALD to that measured before ALD.

S8. Correlative analysis of strain and doping in 1L MoS_2

The following analysis has been previously performed by other authors for graphene [9-13] and more recently 1L MoS_2. [8, 14-18] A freestanding MoS_2 monolayer is a good approximation of an ideal strain-free and undoped system. The characteristic $E^1{}_{2g}$ and A_{1g} Raman modes for suspended CVD-synthesised 1L MoS_2 appear at ~385 cm^{-1} and ~405 cm^{-1}, respectively, [16, 19] and are denoted $\omega^0_{E'}$ and $\omega^0_{A'}$. The positions of the $E^1{}_{2g}$ and A_{1g} peaks in the Raman spectrum of a strained and doped 1L MoS_2, $\omega_{E'}$ and $\omega_{A'}$, can be written in terms of the induced biaxial strain, ε, and electron density, n: [16]

$$\omega_{E'} = \omega^0_{E'} - 2\gamma_{E'}\omega^0_{E'}\varepsilon + k_{E'}n \tag{S2}$$

$$\omega_{A'} = \omega^0_{A'} - 2\gamma_{A'}\omega^0_{A'}\varepsilon + k_{A'}n \tag{S3}$$

where $\gamma_{E'}$ and $\gamma_{A'}$ are the Grüneisen parameters for the two characteristic Raman peaks in 1L MoS_2, and $k_{E'}$ and $k_{A'}$ are the corresponding shift rates of the vibrational modes as a function of carrier density, n. The relevant values used in this analysis are detailed in Table S2.

Table S2: Literature values for the Grüneisen parameters and Raman mode shift rates used in the correlative Raman analysis described in this work.

Parameter	**Value**	**Reference**
$\gamma_{E'}$	0.84	Rice *et al.* [20]
$\gamma_{A'}$	0.15	Rice *et al.* [20]
$k_{E'}$ (×10^{-13} cm)	-0.33	Chakraborty *et al.* [21]
$k_{A'}$ (×10^{-13} cm)	-2.22	Chakraborty *et al.* [21]

It follows from Equations S2 and S3, that any shifts in the positions of the characteristic $E^1{}_{2g}$ and A_{1g} Raman modes that result from a given perturbation can be expressed as: [14]

$$\Delta\omega_{E'} = - 2\gamma_{E'}\omega^0_{E'}\varepsilon + k_{E'}n \tag{S4}$$

$$\Delta\omega_{A'} = -2\gamma_{A'}\omega_{A'}^{0}\varepsilon + k_{A'}n \tag{S5}$$

From this linear set of equations, we obtain relations for the strain and doping:

$$\varepsilon = \frac{k_{A'}\Delta\omega_{E'} - k_{E'}\Delta\omega_{A'}}{2\gamma_{A'}\omega_{A'}^{0}k_{E'} - 2\gamma_{E'}\omega_{E'}^{0}k_{A'}} \tag{S6}$$

$$n = \frac{\gamma_{A'}\omega_{A'}^{0}\Delta\omega_{E'} - \gamma_{E'}\omega_{E'}^{0}\Delta\omega_{A'}}{\gamma_{A'}\omega_{A'}^{0}k_{E'} - \gamma_{E'}\omega_{E'}^{0}k_{A'}} \tag{S7}$$

To determine the equation describing the strain isoline at zero doping, we set $n = 0$ and solve the system of Equations S2 and S3. Similarly, we can obtain the analogous equation for the strain-free doping line in the case of $\varepsilon = 0$.

$$\omega_{A'} = \omega_{A'}^{0} + \frac{\gamma_{A'}\omega_{A'}^{0}}{\gamma_{E'}\omega_{E'}^{0}}\left(\omega_{E'} - \omega_{E'}^{0}\right) \tag{S8}$$

$$\omega_{A'} = \omega_{A'}^{0} + \frac{k_{A'}}{k_{E'}}\left(\omega_{E'} - \omega_{E'}^{0}\right) \tag{S9}$$

Hence, we can generate a ε-n grid of strain and doping isolines, with respective gradients of $\frac{\gamma_{A'}\omega_{A'}^{0}}{\gamma_{E'}\omega_{E'}^{0}} = 0.19$ and $\frac{k_{A'}}{k_{E'}} = 6.73$, as shown in Figure S17. The dashed black lines represent the strain isolines and correspond to $\Delta\varepsilon = \pm 0.1$ % variations in the strain. A $\Delta\varepsilon > 0$ is indicative of tensile strain, whereas a negative $\Delta\varepsilon$ signifies compressive strain. Red dashes outline the doping isolines and indicate relative changes in the electron density of $\Delta n = \pm 0.1 \times 10^{13}$ cm^{-2}, where n-type doping is represented by $\Delta n > 0$ and p-type doping is implied by $\Delta n < 0$.

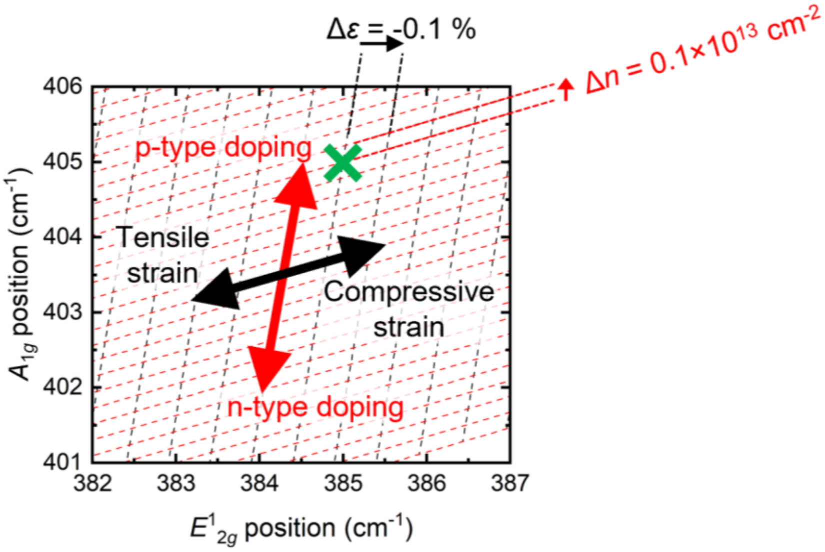

Figure S17: Representative correlative Raman plot of the A_{1g} *Raman peak position as a function of the* E^1_{2g} *Raman peak position, with overlayed ε-n grid of isolines. The directions of the strain and doping effects indicated by the respective isolines are highlighted. The green cross indicates the intersection of the strain-free and undoped isolines at literature values of the Raman peak positions for a suspended CVD-synthesised 1L* MoS_2 *(*E^1_{2g} *~385* cm^{-1} *and* A_{1g} *~405* cm^{-1}*). Changes in strain and electron density relative to this point are indicated.*

References

1. B. Radisavljevic, A. Radenovic, J. Brivio, V. Giacometti and A. Kis, *Nature Nanotechnology*, 2011, **6**, 147-150.
2. A. Splendiani, L. Sun, Y. Zhang, T. Li, J. Kim, C.-Y. Chim, G. Galli and F. Wang, *Nano Letters*, 2010, **10**, 1271-1275.
3. J. Jeon, S. K. Jang, S. M. Jeon, G. Yoo, Y. H. Jang, J.-H. Park and S. Lee, *Nanoscale*, 2015, **7**, 1688-1695.
4. X. Zhang, X.-F. Qiao, W. Shi, J.-B. Wu, D.-S. Jiang and P.-H. Tan, *Chemical Society Reviews*, 2015, **44**, 2757-2785.
5. H. Li, Q. Zhang, C. C. R. Yap, B. K. Tay, T. H. T. Edwin, A. Olivier and D. Baillargeat, *Advanced Functional Materials*, 2012, **22**, 1385-1390.
6. K. Gołasa, M. Grzeszczyk, R. Bożek, P. Leszczyński, A. Wysmołek, M. Potemski and A. Babiński, *Solid State Communications*, 2014, **197**, 53-56.
7. B. F. M. Healy, S. L. Pain, J. Lloyd-Hughes, N. E. Grant and J. D. Murphy, *Materials Research Express*, 2024, **11**, 015002.
8. B. F. M. Healy, S. L. Pain, J. Lloyd-Hughes, N. E. Grant and J. D. Murphy, *Advanced Materials Interfaces*, 2024, **11**, 2400305.
9. T. M. G. Mohiuddin, A. Lombardo, R. R. Nair, A. Bonetti, G. Savini, R. Jalil, N. Bonini, D. M. Basko, C. Galiotis, N. Marzari, K. S. Novoselov, A. K. Geim and A. C. Ferrari, *Physical Review B*, 2009, **79**, 205433.
10. J. E. Lee, G. Ahn, J. Shim, Y. S. Lee and S. Ryu, *Nature Communications*, 2012, **3**, 1024.
11. C. Androulidakis, G. Tsoukleri, N. Koutroumanis, G. Gkikas, P. Pappas, J. Parthenios, K. Papagelis and C. Galiotis, *Carbon*, 2015, **81**, 322-328.
12. A. Armano, G. Buscarino, M. Cannas, F. M. Gelardi, F. Giannazzo, E. Schilirò and S. Agnello, *Carbon*, 2018, **127**, 270-279.
13. E. Schilirò, R. Lo Nigro, S. E. Panasci, F. M. Gelardi, S. Agnello, R. Yakimova, F. Roccaforte and F. Giannazzo, *Carbon*, 2020, **169**, 172-181.
14. A. Michail, N. Delikoukos, J. Parthenios, C. Galiotis and K. Papagelis, *Applied Physics Letters*, 2016, **108**, 173102.
15. W. H. Chae, J. D. Cain, E. D. Hanson, A. A. Murthy and V. P. Dravid, *Applied Physics Letters*, 2017, **111**, 143106.
16. S. E. Panasci, E. Schilirò, G. Greco, M. Cannas, F. M. Gelardi, S. Agnello, F. Roccaforte and F. Giannazzo, *ACS Applied Materials & Interfaces*, 2021, **13**, 31248-31259.
17. E. Schilirò, S. E. Panasci, A. M. Mio, G. Nicotra, S. Agnello, B. Pecz, G. Z. Radnoczi, I. Deretzis, A. La Magna, F. Roccaforte, R. Lo Nigro and F. Giannazzo, *Applied Surface Science*, 2023, **630**, 157476.
18. E. Schilirò, R. L. Nigro, S. E. Panasci, S. Agnello, M. Cannas, F. M. Gelardi, F. Roccaforte and F. Giannazzo, *Advanced Materials Interfaces*, 2021, **8**, 2101117.
19. D. Lloyd, X. Liu, J. W. Christopher, L. Cantley, A. Wadehra, B. L. Kim, B. B. Goldberg, A. K. Swan and J. S. Bunch, *Nano Letters*, 2016, **16**, 5836-5841.
20. C. Rice, R. J. Young, R. Zan, U. Bangert, D. Wolverson, T. Georgiou, R. Jalil and K. S. Novoselov, *Physical Review B*, 2013, **87**, 081307.
21. B. Chakraborty, A. Bera, D. V. S. Muthu, S. Bhowmick, U. V. Waghmare and A. K. Sood, *Physical Review B*, 2012, **85**, 161403.